bioRχiv

Microtubule perturbations of neurite extension and nucleokinesis in an iPSC-derived model system

Muriel Sébastien,[1,2] and Alexandra L. Paquette,[1] Adam G. Hendricks,[2] Gary J. Brouhard[1,✉]
[1]Department of Biology, McGill University, Montréal, Québec, Canada
[2]Department of Bioengineering, McGill University, Montréal, Québec, Canada
✉Correspondence should be addressed to M.S. (muriel.sebastien@mcgill.ca) or G.J.B. (gary.brouhard@mcgill.ca)

Microtubules in neurons can be characterized based on their dynamic behavior (dynamic vs. stable), on their point of origin (centrosomal vs. acentrosomal), on their relative orientation (parallel vs. antiparallel), and a range of other features. Patterns of different microtubule types are essential in neurite extension and neuronal migration. Cellular model systems such as rodent primary cultures and iPSC-derived neurons have provided key insights into how these patterns are created and maintained through the action of microtubule associated proteins (MAPs), motor proteins, and regulatory enzymes. Here we have characterized a recent cellular model based on induced pluripotent stem cells (iPSC)-derived neurons (EBiSC-NEUR1 neurons), in which doxycycline-induced expression of Neurogenin-2 drives consistent trans-differentiation into the neuronal state. We measured the process extension and nucleokinesis of NEUR1 neurons, which are comparable to published data from primary cultures and other iPSC-based models. We challenged NEUR1 neurons with a panel of drugs modifying microtubule physiology. NEUR1 extension and nucleokinesis were significantly perturbed by two microtubule-targeting drugs, namely a taxane (paclitaxel) and a vinca alkaloid (DZ-2384). In contrast, inhibition of microtubule severing (spastazoline) or of deacetylation (trichostatin A) had a limited effect on nucleokinesis only. Our results support the primary importance of microtubule dynamics in neuronal development and demonstrate the power of NEUR1 neurons as a model system.

Introduction

More than 60 years after the discovery of microtubules in plant cells (*1*), researchers continue to discover new and diverse characteristics of these indispensable polymers. Key among these characteristics is dynamic instability (*2*), or the capacity of microtubule ends to switch rapidly between growth and shrinkage ("catastrophes" and "rescues"). Cells can increase the rates of this switching behavior, e.g., when microtubule plus ends become highly dynamic during mitosis (*3-6*). Alternatively, cells can suppress dynamics, creating microtubules that are long-lived, stable, and resistant to mechanical damage (*4, 7-9*). Both stable and dynamic subsets of microtubules exist side-by-side and are found in diverse geometric arrangements, especially parallel bundles, anti-parallel bundles, and asters (*10*). These complex networks are built and maintained by a host of microtubule-associated proteins (MAPs) (*11*), motor proteins (*12, 13*), and regulatory enzymes (*14*). The coordinated action of these MAPs, motors, and enzymes will construct and functionalize a microtubule cytoskeleton that meets each differentiated cell's needs (*15*).

Neurons have evolved a particularly sophisticated microtubule network, given their need to extend many neurites / processes, functionalize an axon and dendrites, and transport cargos over great distances (*16, 17*). As neurons develop, they express several isoforms of α-tubulin, as well as a specific isoform of β-tubulin (β3-tubulin, Tubb3 in humans) (*18*). Many of these isoforms are implicated in brain disease when mutated (*19, 20*). In addition, neurons accumulate several post-translational modifications (PTMs; one component of the "tubulin code" (*21*)), such as polyglutamate chains on αβ-tubulin's disordered C-termini, and acetylation on α-tubulin in the microtubule lumen. Remarkably, distinct PTMs can be found in anti-parallel bundles, an arrangement that may play a critical role in cargo sorting (*22*). Patterns of neuronal microtubules can also be distinguished by their points of origin, which include the centrosome early in development (*23*) as well as acentrosomal sites such as Golgi outposts (*24, 25*). The centrosomal microtubules are necessary for the radial migration of cortical neurons, but not for axon formation (*26, 27*), indicating distinct roles for centrosomal vs. acentrosomal microtubules in the life cycle of these neurons. Presumably then, microtubules within neurons are distinct at the molecular level, in terms of their relative dynamics, their specific cohort of MAPs, their range of PTMs, etc. But we cannot yet draw a complete molecular map of how microtubule subsets emerge, maintain distinction, and subsequently drive neuronal development (*17*).

To study neuronal microtubule networks at the molecular level, model systems include primary cultures from rodents (*28, 29*), model organisms such as *C. elegans* and *D. melanogaster* (*30, 31*), and recently developed models based on human induced pluripotent stem cells (iPSCs) (*32*). The use of human iPSCs shows promise for disease modeling (*33, 34*), particularly when combined with CRISPR/Cas9 genome editing techniques (*35-37*). For example, CRISPR-modified iPSCs could be induced first into neural progenitor cells (NPCs) using small molecules like SMAD inhibitors (later referred to as SMADi (*38*)) and then differentiated into neuronal subtypes with specific growth factor supplementation (*39*). We recently developed a model for X-linked lissencephaly using SMADi-inducible iPSCs that carry mutations in the *DCX* gene and were differentiated into cortical neurons (*40*). The induction into NPCs with SMADi requires approximately 30 days of time and media, however. More recently, trans-differentiation approaches were developed wherein iPSCs were engineered to express the neural

lineage transcription factor Neurogenin-2 (NGN2) under a doxycycline inducible promotor (*41-44*). Doxycycline treatment drives consistent induction of all iPSCs into neural lineage in only a couple of days. Then, terminal differentiation into specific neuronal subtypes can be achieved as before, using specific factors. Multiple studies investigating microtubule dynamics and cargo transport using these neurons demonstrated their promise for studying the microtubule network (*45-47*), but their physiology remains incompletely characterized.

In the present study, we characterized neurite extension and nucleokinesis in EBiSC-NEUR1 iPSCs-derived neurons (hereafter referred as NEUR1), a fast-inducible NGN2 iPSC line (*41*) obtained from the European Bank of induced pluripotent Stem Cells (EBiSC). We find that NEUR1 neurons extend neurites at rates comparable to primary rodent cultures and other iPSC models, and NEUR1 nuclei show robust translocation and migratory behavior. We challenged NEUR1 neurons with a panel of small molecules that disrupt microtubule dynamics, target a microtubule severing enzyme, or alter the balance of tubulin acetylation. We find that subsets of stable and dynamic microtubules are essential for process extension and nucleokinesis. Overall, our work contributes to the development of iPSC-based cellular models for the neuronal microtubule cytoskeleton.

Results and discussion

NEUR1 neurons extend an arbor of neurites enriched in β3-tubulin

We began with a baseline characterization of NEUR1 neurons differentiated into cortical neurons. These neurons were obtained from induced NGN2 expression with doxycycline for 2 days prior to long-term cryopreservation; aliquots of frozen cells were thawed directly into terminal differentiation media supplemented with doxycycline at t = 0 of the experiment (Fig. 1A). To characterize the development of NEUR1 neurons over the next 7 days, we examined their morphology and microtubule content using methods previously established for a SMADi-inducible line (CTRL0 in (*40*)). In nearly every cell we observed robust development of neuronal processes, an elongated morphology, and positive staining for the neuronal-specific β3-tubulin, Tubb3, as expected (*48, 49*). In contrast, SMADi-inducible cultures sometimes contain non-neuronal cells and/or proliferating NPCs, even in terminal differentiation media, and thus require additional quality control and care. Figure 1B shows an immunocytochemistry image of Tubb3 staining at day 3 and day 7, and the length of neurites increased significantly over this time period. To quantify this increase, we skeletonized the tubulin images and measured the total length of the neurite network per cell (or arborization length, see Methods). The arborization length increased from 203.68 ± 5.16 µm at 3 days to 433.22 ± 16.73 µm at 7 days (Fig. 1B, mean ± SEM, p<0.0001, ***). This increase in arborization lengths is comparable to lengths measured in rodent neurons (*50-52*) and in other iPSC models (*40, 53*), which is on the order of a hundred micrometers per day. Increased arborization is typically accompanied by increased expression of Tubb3 and increased PTM levels. To confirm these predictions, we generated Western blots using antibodies against Tubb3 and acetylated tubulin (Acetyl). Both antibody signals increased significantly from day 3 to day 7, with an approximately 30% increase in Tubb3 signal and a 70% increase in Acetyl signal over that time period (Fig 1C).

From these findings, we conclude that NEUR1 iPSCs differentiate and mature into cortical neurons that compare

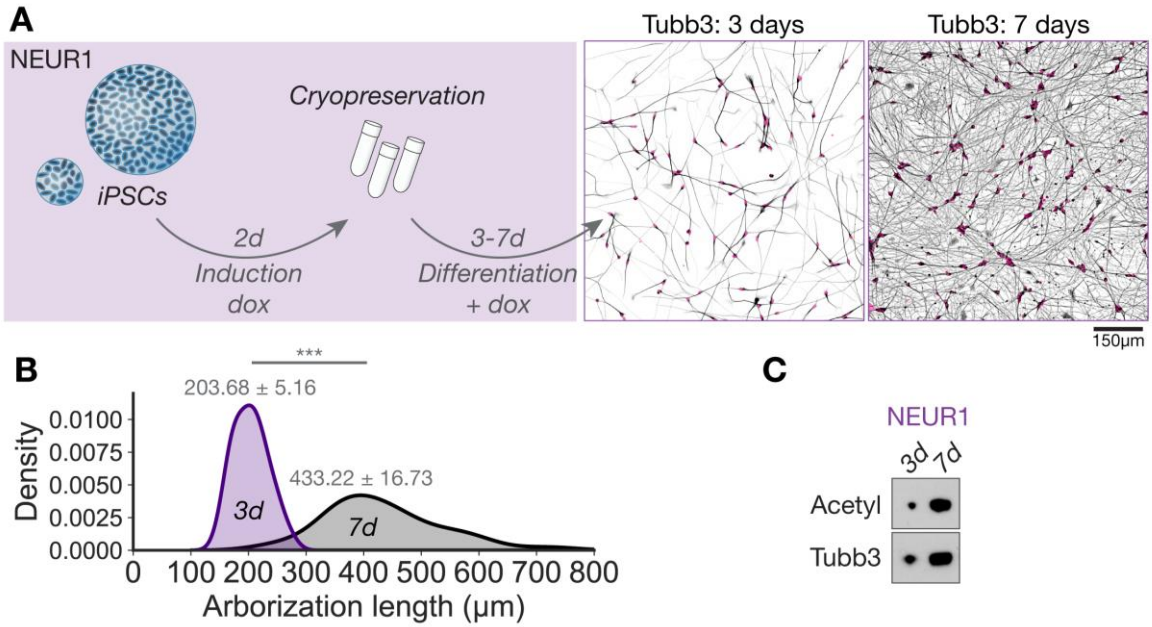

Figure 1: NEUR1 neurons extend an arbor of neurites enriched in β3-tubulin. (A) Left panel: Schematics of induction and differentiation process in NEUR1 lines from iPSCs aggregates to early neuronal stages. NEUR1 iPSCs were induced for 2 days in Neurobasal media supplemented with doxycycline (dox) before cryopreservation, shipping and usage. The early neurons were thawed in BrainPhys + dox and terminally differentiated for 3-7 days. Right panels: Representative images of Tubb3 immunostaining of NEUR1 neurons at 3 days and 7 days of differentiation. Nuclei are pseudo-colored in magenta. **(B)** Distribution of neurite arborization length per cell body in NEUR1 neurons at 3 days (3d) and 7 days (7d) of differentiation. N=868-4181 neurons from at least 2 independent experiments. The mean values ± SEM for each condition are detailed on the plot. Statistical analysis was done using Mann-Whitney non-parametric tests: *** p<0.001. **(C)** Representative immunoblots of tubulin acetylation (611B1) and Tubb3 in NEUR1 neurons at 3 (3d) and 7 days (7d) of differentiation.

favorably to rodent cultures and other iPSC models. In particular, the relative homogeneity of NEUR1 neurons make them well-suited to screening applications and automated image analysis, e.g. of cell morphology and nucleokinesis.

NEUR1 neurons exhibit robust nucleokinesis

Nucleokinesis is also a critical process in neurodevelopment, so we analyzed NEUR1 neurons using a previously established nuclear translocation assay (*40*). The cells were seeded at a density of 15000 cells/cm^2, differentiated for 3 days, stained with Syto™ nuclear dye, and imaged for 5h (See supplemental movies). We observed robust nuclear movements over the full time-course of imaging. Figure 2A and 2B show representative still images of the cells' morphologies and nuclear stain, with nuclear trajectories overlayed as purple lines. We quantified nuclear movements using an automated tracking pipeline (*40*). Trajectories were filtered and analyzed to determine the mean speed, the total distance traveled, and directionality index (efficiency of displacement, see Methods). Figure 2C shows a sample of these extracted trajectories (n=1764), which are color-coded according to

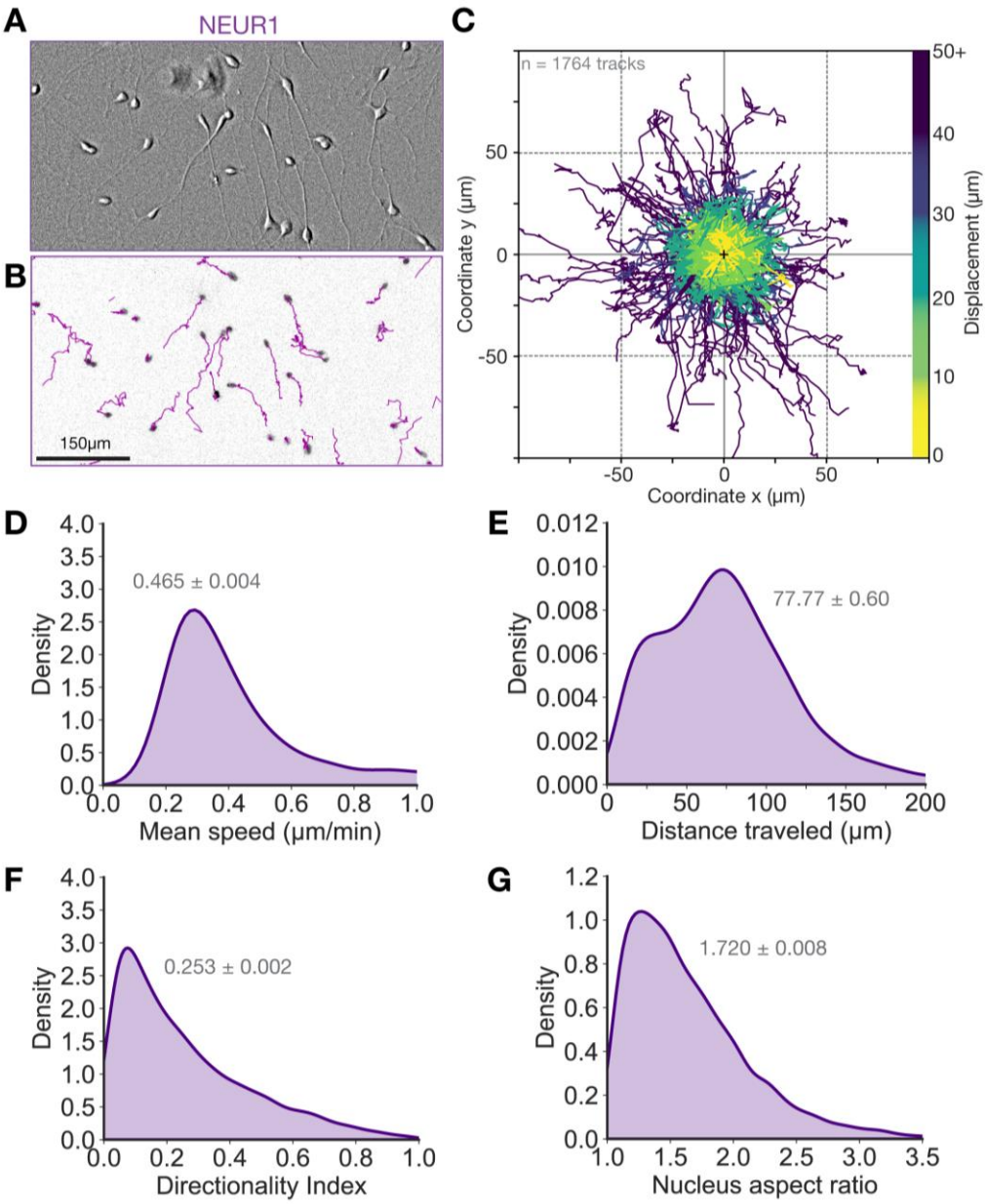

Figure 2: NEUR1 neurons exhibit robust nucleokinesis. (A) Representative image of NEUR1 neurons at 3 days of differentiation by brightfield imaging, showing neuronal morphology at the start of the tracking experiment. **(B)** Still image of nuclei stained with 250nM Syto™ deep red for the neurons shown in panel A. Results of the automated tracking over a 5h-time period are showed as overlayed tracks in purple. **(C)** Position plots of 1764 sample tracks for NEUR1 nuclei. Each track is color-coded according to its displacement (see color scale on the right). **(D)** Distribution of mean speed for NEUR1 neurons at 3 days of differentiation. The plot was cut **(E)** Distribution of distance traveled for NEUR1 neurons at 3 days of differentiation. **(F)** Distribution of directionality index for NEUR1 neurons at 3 days of differentiation. For D-F) Tracks that lasted less than 30min were excluded from the analysis (see methods). n=6527 NEUR1 neurons, from 3 independent experiments. Mean values ± SEM are displayed on each plot. The plots were cut-off to better show the main populations, but the maximum values for mean speed and distance traveled are 2.865 µm/min and 390.80 µm respectively. Statistical analysis was done using Kruskal-Wallis non-parametric test: *** p<0.001. **(G)** Distribution of nucleus aspect ratios for NEUR1 neurons at 3 days of differentiation. n=4095 NEUR1 nuclei, from 3 independent experiments. Mean values ± SEM are displayed on the plot. This plot was cut-off to better show the main population, the maximal value for Nucleus aspect ratio is 5.556. Statistical analysis was done using Mann-Whitney non-parametric tests: ns non-significant, *** p<0.001.

their total displacement (see scale, right). NEUR1 nuclei covered considerable distance over the 5 h imaging period (Fig. 2E) and moved slightly faster (0.465 ± 0.004 µm/min, Fig. 2D) than migrating iPSC-derived neurons in organoids (*54*). The directionality index was 0.253 ± 0.002, however, implying that movements are more meandering than directed (Fig. 2F). In addition, we measured the aspect ratio of the nuclei in DAPI stainings, and found that NEUR1 nuclei were slightly elongated (Fig. 2G), possibly due to cytoskeletal forces exerted on the nucleus during nucleokinesis.

As with differentiation and neurite extension, our results on nucleokinesis compare favorably with other iPSC-based models (*54*) and with rodent cultures (*55, 56*), making NEUR1 neurons an excellent model system for studying early stages of neuronal development and the underlying functions of the microtubule cytoskeleton.

NEUR1 morphology is disrupted by some, but not all, drug-based challenges

Both arborization and nucleokinesis require a sophisticated microtubule network divided into distinct, functional patterns. Thus, we wondered how NEUR1 development would respond to disruptions to the microtubule cytoskeleton when challenged with four different drugs. Two drugs target microtubules directly (a taxane, paclitaxel; and a vinca alkaloid, the Diazonamide-A derivative DZ-2384), and two drugs target microtubules indirectly (an inhibitor of the severing enzyme spastin, spastazoline; and an inhibitor of a PTM pathway, trichostatin A). We incubated NEUR1 cortical neurons with each drug for 7 hours prior to analysis on day 3. To analyze morphology and cell density, the neurons were fixed and stained for DAPI and Tubb3, and immunocytochemistry images were processed and analyzed as described above.

Both drugs that target microtubules directly caused significant reductions in arborization lengths. Treatment with 100 nM paclitaxel caused the neurons to have shorter, curvier neurites, as if they were more flexible than control neurites (Fig. 3A). Paclitaxel binds to microtubules at their taxane sites, located in the lateral loops of β-tubulin in the microtubule lumen (*57*). This interaction creates structure in the lateral loops (*58*) and "expands" the microtubule lattice(*59*). These changes act to stabilize the microtubules but also to reduce their persistence lengths (*4, 9*). The 100 nM paclitaxel treatment did not appear to affect cell density, as measured by the number of nuclei per field of view (Fig. 3B), but treated neurons had a significantly reduced

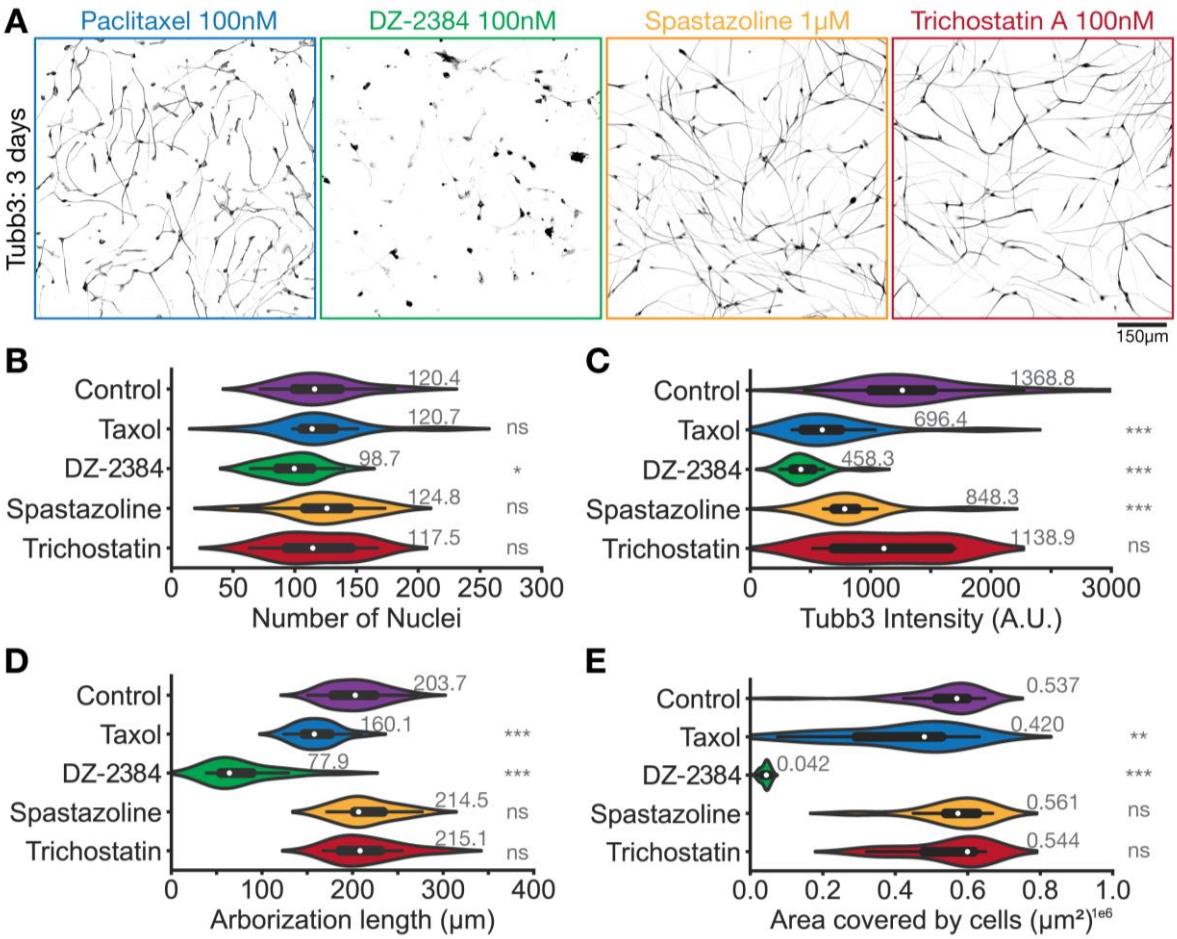

Figure 3: Microtubule dynamics are necessary for proper neuronal morphology. (A) Representative images of Tubb3 stainings in 7h drug treated NEUR1 neurons at 3 days of differentiation. **(B)** Distribution of number of nuclei per field of view in control and drug treated NEUR1 neurons at 3 days of differentiation. **(C)** Distribution of Tubb3 intensity per field of view in control and drug treated NEUR1 neurons at 3 days of differentiation. This plot was cut-off to better show the main population, the maximal value for Tubb3 intensity is 3156.4 A.U. **(D)** Distribution of neurite arborization length per cell body in control and drug treated NEUR1 neurons at 3 days of differentiation. n = 1410-4095 neurons, from 3 independent experiments. **(E)** Distribution of the area covered by cells or Tubb3 staining in control and drug treated NEUR1 neurons at 3 days of differentiation. 1e6 means values represented should be multiplied by 10^6. For B-E) mean values are detailed next to the violins. n = 12-34 field of views, from 3 independent experiments. Statistical analysis was done using Mann-Whitney non-parametric tests: ns non-significant, * $p<0.05$, *** $p<0.001$.

arborization length (Control: 203.68 ± 5.16 vs paclitaxel: 160.08 ± 6.00 µm, $p<0.001$, ***, Fig. 3C). We also observed a reduced intensity of Tubb3 staining (Fig. 3D), indicating either reduced expression of this isotype or overall reduced polymer levels (note: our fixation protocols include an extraction step that should remove soluble tubulin). The Tubb3 signal also covered a smaller area within the field of view (Fig. 3E), consistent with the reduced arborization length measured by skeletonization.

We observed similar, albeit stronger effects with DZ-2384 (*60-62*). Treatment with 100 nM DZ-2384 caused a sharp reduction in arborization length (Control: 203.68 ± 5.16 vs DZ-2384: 77.89 ± 9.81 µm, $p<0.001$, ***, see Fig. 3D), in Tubb3 signal (Fig. 3C), as well as Tubb3 area (Fig. 3E). DZ-2384 binds the vinca-alkaloid site, located at the interdimer interface of protofilaments, forcing the tubulin oligomers to adopt a curved conformation (*62*). Such oligomers prevent polymerization and/or promote destabilization of microtubule ends, typically leading to microtubule depolymerization, consistent with our findings. DZ-2384 also significantly reduced the number of nuclei per field of view (Fig. 3B), suggesting that this treatment causes cell detachment and/or cell death. These results demonstrate that direct disruptions to microtubule dynamics significantly changed neuronal morphology on short time scales, regardless of the specific drug employed.

In contrast, spastazoline and trichostatin A, which target microtubules indirectly, did not affect neuronal morphology. We treated neurons with 1 µM spastazoline, an inhibitor of the microtubule severing enzyme, spastin (*63, 64*) and no morphological changes to neurons were apparent. Although its role(s) in neuronal development remain unclear, spastin localizes to neuronal branching points and has been proposed to sever long microtubules, thus generating short, dynamic microtubules that drive branch formation (*65, 66*). Alternatively, spastin may catalyze the turnover of tubulin within the microtubule shaft by creating damage in the lattice that is subsequently repaired (*67*). In either case, the 1 µM spastazoline treatment did not significantly change arborization length (Control: 203.68 ± 5.16 vs spastazoline: 214.51 ± 8.71 µm, $p=0.33$, ns, see Fig. 3D), cell density (Fig. 3B), or the area covered by Tubb3 signal (Fig. 3E). We did measure a reduced Tubb3 signal intensity (Fig. 3C), indicating the drug-based challenge was disruptive, but this reduced intensity did not translate into measurable morphological changes.

Finally, we challenged the microtubule network of NEUR1 neurons by targeting a PTM pathway, namely acetylation. Acetylation occurs mostly at lysine 40 (K40) of α-tubulin, which is located in the microtubule lumen (*68*). The modification is reversible, and the levels of K40 acetylation reflect the balance of activity of acetylases (e.g., αTAT1) and de-acetylases. Once acetylated, microtubules are more stable and resistant to mechanical damage (*4, 9*). To increase acetylation levels, we treated NEUR1 neurons with 100 nM trichostatin A, an inhibitor of histone deacetylase 6 (HDAC6). As its name indicates, HDAC6 can deacetylate histones as well as K40 α-tubulin (*68*). Similar to spastazoline, trichostatin A did not significantly affect arborization length (Control: 203.68 ± 5.16 vs trichostatin A: 215.13 ± 10.64 µm, $p=0.45$, ns, see Fig. 3D), cell density (Fig. 3B), or Tubb3 area (Fig. 3E), and no morphological changes were observed (Fig. 3A). We also did not observe changes in Tubb3 intensity (Fig. 3C). These results indicate that increased acetylation levels are not sufficient to modify the morphology of NEUR1 neurons in a measurable way, at least under the conditions of our experiments. It remains possible that NEUR1 neurons would respond to longer incubation times or an earlier challenge, but further experiments would be needed to completely exhaust these options.

Overall, these results confirm that disrupting microtubule dynamics directly with paclitaxel or DZ-2384 has a strong and rapid effect on NEUR1 morphology. In contrast, increasing acetylation levels with trichostatin A or reducing Tubb3 signal intensity with spastazoline alone does not. Thus, the maintenance of a balance between stable and dynamic microtubule populations is critical in NEUR1 neurons, as in many other model systems.

Changes in nuclear movements correlate with changes in morphology

Next, we wondered whether these changes in NEUR1 morphology would correlate with changes in nucleokinesis. To that end, we analyzed NEUR1 nuclear movements over a 5h time-period in the presence of our panel of drugs. Figure 4A and Figure 4B show representative images and tracking results for each condition, while Figure 4C shows a sample of extracted tracks (n = 1322-1742 tracks per condition). As described previously, we measured the characteristics of these trajectories (e.g. mean speed); the distributions of these features are shown as violin plots in Figure 4D-G. Overall, each drug condition that we tested had a significant effect on at least some, if not all, characteristics of nucleokinesis.

Similar to the analysis of NEUR1 morphology (Fig. 3), the most visible differences in nuclear translocation were observed in the paclitaxel and DZ-2384 conditions. However, unlike the morphology results, these two direct microtubule-targeting drugs differed significantly in terms of their impact. Paclitaxel treatment inhibited nuclear movements, while DZ-2384 treatment seemed to exaggerate them. More precisely, paclitaxel treatment resulted in reduced mean speed, (Control: 0.465 ± 0.004 µm/min vs Taxol: 0.373 ± 0.004 µm/min, $p<0.001$, ***, Fig. 4D), reduced distance traveled (Fig. 4E), and a lower directionality index (Fig. 4F). In addition, the nuclei were rounder than in control conditions (Fig. 4G), consistent with nuclei that are experiencing reduced cytoskeletal forces (reduced persistence length).

In contrast, DZ-2384 treatment resulted in higher mean speed (Control: 0.465 ± 0.004 µm/min vs DZ-2384: 0.587 ± 0.004 µm/min, $p<0.001$, ***, Fig. 4D), longer distance traveled (Fig. 4E), and increased directionality (Fig. 4F). Surprisingly, when looking at the nuclear shape, we found that DZ-2384-treated nuclei were rounder than control ones (Fig. 4G), suggesting there are no cytoskeletal forces applied to them. One hypothesis could be that microtubule depolymerization induced by DZ-2384 leads to detachment of neurite tips and subsequent retraction of neurites. These results emphasize the importance of dynamic and stable

microtubule populations for nuclear translocation and therefore neuronal migration.

Interestingly, whereas spastazoline had a minimal effect on arborization length (Fig. 3D), its influence on nuclear movement was more pronounced. For example, spastazoline treatment resulted in reduced mean speed, (Control: 0.465 ± 0.004 µm/min vs spastazoline: 0.394 ± 0.003 µm/min, $p<0.001$, ***, Fig. 4D), reduced distance traveled (Fig. 4E), and a rounding of nuclear shape (Fig. 4G). This result is reminiscent of the data showing that disruption of centrosomal microtubules significantly affected nuclear migration in rodent cortical projection neurons (*27*). We can speculate that spastin may have a

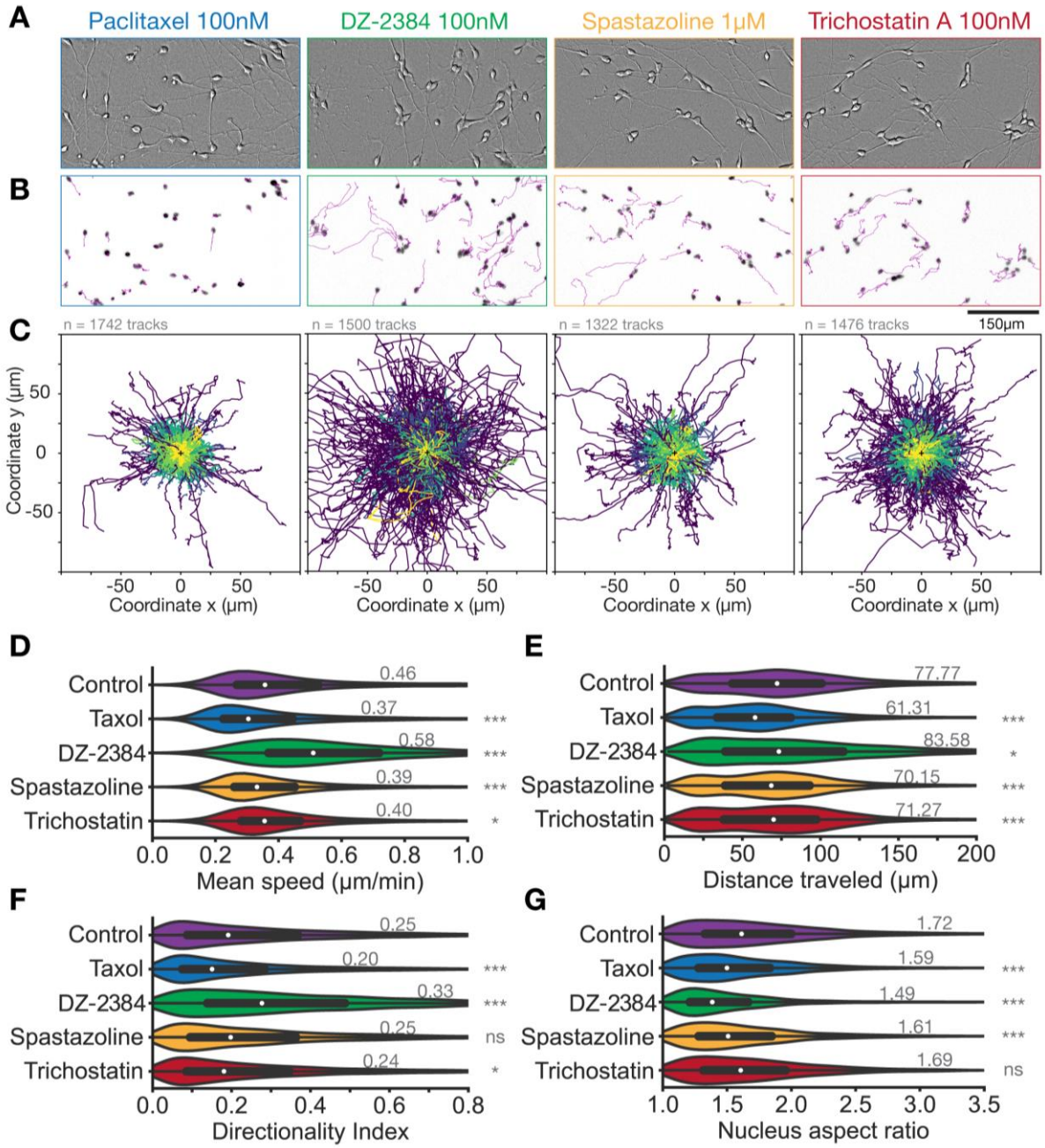

Figure 4: Changes in nuclear movements correlate with changes in morphology. A) Representative still brightfield images of control and treated NEUR1 neurons at 3 days of differentiation, showing neuronal morphology at the start of the tracking experiment. **B)** Representative still images of nuclei stained with Syto™ deep red for control and drug treated NEUR1 neurons at 3 days of differentiation. Results of the automated tracking over a 5h-time period are showed as overlayed tracks for all conditions. **C)** Position plots of 1742, 1500, 1322, and 1476 sample tracks for paclitaxel, DZ-2384, spastazoline and trichostatin treated NEUR1 nuclei respectively. Each track is color-coded according to its displacement (see color scale Fig2C). **D)** Distribution of mean speed for control and treated NEUR1 nuclei at 3 days of differentiation. **E)** Distribution of distance traveled for control and treated NEUR1 nuclei at 3 days of differentiation. **F)** Distribution of directionality index for control and treated NEUR1 nuclei at 3 days of differentiation. For D-F) n=3859-6527 nuclear tracks from 3 independent experiments. These plots were cut-off to better show the main populations, maximal values are: control mean speed 2.865 µm/min, trichostatin distance traveled 434.76 µm and 1.0 for directionality index with all conditions. Statistical analysis was done using Kruskal-Wallis non-parametric tests: ns non-significant, * $p<0.05$, *** $p<0.001$. **G)** Distribution of nuclei aspect ratios for control and treated NEUR1 neurons at 3 days of differentiation. n = 1410-4095 nuclei, from 3 independent experiments. This plot was cut-off to better show the main population, the maximal value for Nucleus aspect ratio is 5.556 in the control condition. Statistical analysis was done using Mann-Whitney non-parametric tests: ns non-significant, *** $p<0.001$.

different impact on centrosomal vs. acentrosomal subsets of microtubules, although this idea requires testing.

Unlike the other drugs, trichostatin A had a minimal impact on both cell morphology and nucleokinesis. Trichostatin A treatment resulted in a small reduction in mean speed (Control: 0.465 ± 0.004 µm/min vs trichostatin A: 0.402 ± 0.003 µm/min, $p<0.05$, *, Fig. 4D), distance traveled (Fig. 4E) and directionality (Fig. 4F), but overall trichostatin A nuclei were the most statistically similar to control. These minimal effects on NEUR1 nuclei support a hypothesis wherein acetylation of α-tubulin K40 is not relevant for nucleokinesis. Alternatively, we cannot exclude that phenotypes would manifest with longer drug treatments, although we do note that a significant increase in K40 acetylation is detectable in our time window (Fig. S1). Current models for the role of K40 acetylation suggest it plays a role in the regulation of intracellular trafficking, particularly pre-synaptic cargos (*69, 70*). However, such regulation may only become critical at later stages of development than those analysed here.

Altogether, our data indicates that NEUR1 nucleokinesis is sensitive to a wider range of drugs than NEUR1 morphology. The drug-based challenges to the NEUR1 cytoskeleton suggest that the maintenance of dynamic and stable microtubules is critical to proper development in this model system. Moreover, the spastin disruption by spastazoline implies some distinction between nucleokinesis and process extension, supporting the existing model that distinct subsets of microtubules are required for each of these developmental steps(*27*).

Concluding remarks

We have characterized the morphology and nucleokinesis of the latest generation of iPSC-derived neurons using doxycycline-induced expression of NGN2 to bypass the time-consuming process of inducing iPSCs into neural progenitor cells. Terminal differentiation of NEUR1 neurons into cortical neurons produced cultures that were homogenous, well-behaved, and thus perfectly tailored for drug screening studies and high-throughput data acquisition. Our study contributes to the build-out of this important model system through the comprehensive measurement of their process extension and nucleokinesis. We find that NEUR1 neurons compare favorably to primary rodent cultures as well as previously described iPSC systems, and we are optimistic about their potential as a robust model system for the neuronal microtubule cytoskeleton. When the NEUR1 cytoskeleton was challenged by drug compounds, the results underlined the importance of distinct patterns of microtubules in neuronal development (dynamic vs. stable, centrosomal vs. acentrosomal). We anticipate that iPSC-based cellular models will play a critical role in mapping out the molecular mechanisms by which neurons establish their complex cytoskeletons.

References

1. M. C. Ledbetter, K. R. Porter, A "Microtubule" in Plant Cell Fine Structure. *J Cell Biol* **19**, 239-250 (1963).
2. T. Mitchison, M. Kirschner, Dynamic instability of microtubule growth. *Nature* **312**, 237-242 (1984).
3. W. M. Saxton *et al.*, Tubulin dynamics in cultured mammalian cells. *J Cell Biol* **99**, 2175-2186 (1984).
4. D. Portran, L. Schaedel, Z. Xu, M. Thery, M. V. Nachury, Tubulin acetylation protects long-lived microtubules against mechanical ageing. *Nat Cell Biol* **19**, 391-398 (2017).
5. L. D. Belmont, A. A. Hyman, K. E. Sawin, T. J. Mitchison, Real-time visualization of cell cycle-dependent changes in microtubule dynamics in cytoplasmic extracts. *Cell* **62**, 579-589 (1990).
6. N. M. Rusan, C. J. Fagerstrom, A. M. Yvon, P. Wadsworth, Cell cycle-dependent changes in microtubule dynamics in living cells expressing green fluorescent protein-alpha tubulin. *Mol Biol Cell* **12**, 971-980 (2001).
7. A. Lieuvin, J. C. Labbe, M. Doree, D. Job, Intrinsic microtubule stability in interphase cells. *J Cell Biol* **124**, 985-996 (1994).
8. Y. Li, M. M. Black, Microtubule assembly and turnover in growing axons. *J Neurosci* **16**, 531-544 (1996).
9. Z. Xu *et al.*, Microtubules acquire resistance from mechanical breakage through intralumenal acetylation. *Science* **356**, 328-332 (2017).
10. R. Subramanian, T. M. Kapoor, Building complexity: insights into self-organized assembly of microtubule-based architectures. *Dev Cell* **23**, 874-885 (2012).
11. S. Bodakuntla, A. S. Jijumon, C. Villablanca, C. Gonzalez-Billault, C. Janke, Microtubule-Associated Proteins: Structuring the Cytoskeleton. *Trends Cell Biol* **29**, 804-819 (2019).
12. N. Hirokawa, R. Takemura, Molecular motors and mechanisms of directional transport in neurons. *Nat Rev Neurosci* **6**, 201-214 (2005).
13. S. E. Cason, E. L. F. Holzbaur, Selective motor activation in organelle transport along axons. *Nat Rev Mol Cell Biol* **23**, 699-714 (2022).
14. C. Janke, M. M. Magiera, The tubulin code and its role in controlling microtubule properties and functions. *Nat Rev Mol Cell Biol* **21**, 307-326 (2020).
15. A. Akhmanova, L. C. Kapitein, Mechanisms of microtubule organization in differentiated animal cells. *Nat Rev Mol Cell Biol* **23**, 541-558 (2022).
16. C. Conde, A. Caceres, Microtubule assembly, organization and dynamics in axons and dendrites. *Nat Rev Neurosci* **10**, 319-332 (2009).
17. M. K. Iwanski, L. C. Kapitein, Cellular cartography: Towards an atlas of the neuronal microtubule cytoskeleton. *Front Cell Dev Biol* **11**, 1052245 (2023).
18. Y. Q. Jiang, M. M. Oblinger, Differential regulation of beta III and other tubulin genes during peripheral and central neuron development. *J Cell Sci* **103 (Pt 3)**, 643-651 (1992).
19. M. A. Tischfield *et al.*, Human TUBB3 mutations perturb microtubule dynamics, kinesin interactions, and axon guidance. *Cell* **140**, 74-87 (2010).
20. N. Bahi-Buisson *et al.*, The wide spectrum of tubulinopathies: what are the key features for the diagnosis? *Brain* **137**, 1676-1700 (2014).
21. K. J. Verhey, J. Gaertig, The tubulin code. *Cell Cycle* **6**, 2152-2160 (2007).
22. R. P. Tas *et al.*, Differentiation between Oppositely Oriented Microtubules Controls Polarized Neuronal Transport. *Neuron* **96**, 1264-1271 e1265 (2017).
23. W. Yu, V. E. Centonze, F. J. Ahmad, P. W. Baas, Microtubule nucleation and release from the neuronal centrosome. *J Cell Biol* **122**, 349-359 (1993).
24. K. M. Ori-McKenney, L. Y. Jan, Y. N. Jan, Golgi outposts shape dendrite morphology by functioning as sites of acentrosomal microtubule nucleation in neurons. *Neuron* **76**, 921-930 (2012).
25. M. M. Fu *et al.*, The Golgi Outpost Protein TPPP Nucleates Microtubules and Is Critical for Myelination. *Cell* **179**, 132-146 e114 (2019).
26. M. Stiess *et al.*, Axon extension occurs independently of centrosomal microtubule nucleation. *Science* **327**, 704-707 (2010).
27. S. Vinopal *et al.*, Centrosomal microtubule nucleation regulates radial migration of projection neurons independently of polarization in the developing brain. *Neuron* **111**, 1241-1263 e1216 (2023).
28. L. Peris *et al.*, Tubulin tyrosination regulates synaptic function and is disrupted in Alzheimer's disease. *Brain* **145**, 2486-2506 (2022).
29. M. M. Magiera *et al.*, Excessive tubulin polyglutamylation causes neurodegeneration and perturbs neuronal transport. *EMBO J* **37**, (2018).
30. D. Puri *et al.*, Wnt signaling establishes the microtubule polarity in neurons through regulation of Kinesin-13. *J Cell Biol* **220**, (2021).

31. M. A. H. Jakobs, A. Zemel, K. Franze, Unrestrained growth of correctly oriented microtubules instructs axonal microtubule orientation. *Elife* **11**, (2022).
32. K. Takahashi, S. Yamanaka, Induction of pluripotent stem cells from mouse embryonic and adult fibroblast cultures by defined factors. *Cell* **126**, 663-676 (2006).
33. J. T. Dimos *et al.*, Induced pluripotent stem cells generated from patients with ALS can be differentiated into motor neurons. *Science* **321**, 1218-1221 (2008).
34. I. H. Park *et al.*, Disease-specific induced pluripotent stem cells. *Cell* **134**, 877-886 (2008).
35. M. Jinek *et al.*, A programmable dual-RNA-guided DNA endonuclease in adaptive bacterial immunity. *Science* **337**, 816-821 (2012).
36. K. Takahashi, S. Yamanaka, A decade of transcription factor-mediated reprogramming to pluripotency. *Nat Rev Mol Cell Biol* **17**, 183-193 (2016).
37. A. McTague, G. Rossignoli, A. Ferrini, S. Barral, M. A. Kurian, Genome Editing in iPSC-Based Neural Systems: From Disease Models to Future Therapeutic Strategies. *Front Genome Ed* **3**, 630600 (2021).
38. S. M. Chambers *et al.*, Highly efficient neural conversion of human ES and iPS cells by dual inhibition of SMAD signaling. *Nat Biotechnol* **27**, 275-280 (2009).
39. A. J. Hulme, S. Maksour, M. St-Clair Glover, S. Miellet, M. Dottori, Making neurons, made easy: The use of Neurogenin-2 in neuronal differentiation. *Stem Cell Reports* **17**, 14-34 (2022).
40. M. Sébastien, E. N. P. Prowse, A. G. Hendricks, G. J. Brouhard, Doublecortin regulates neuronal migration by editing the tubulin code. *bioRxiv*, 2023.2006.2002.543327 (2023).
41. J. Wihan *et al.*, Production of Human Neurogenin 2-Inducible Neurons in a Three-Dimensional Suspension Bioreactor. *J Vis Exp*, (2023).
42. B. Schmid *et al.*, Generation of two gene edited iPSC-lines carrying a DOX-inducible NGN2 expression cassette with and without GFP in the AAVS1 locus. *Stem Cell Res* **52**, 102240 (2021).
43. J. Gu, B. Rollo, H. Sumer, B. Cromer, Targeting the AAVS1 Site by CRISPR/Cas9 with an Inducible Transgene Cassette for the Neuronal Differentiation of Human Pluripotent Stem Cells. *Methods Mol Biol* **2495**, 99-114 (2022).
44. M. S. Fernandopulle *et al.*, Transcription Factor-Mediated Differentiation of Human iPSCs into Neurons. *Curr Protoc Cell Biol* **79**, e51 (2018).
45. A. Dema, R. Charafeddine, S. Rahgozar, J. van Haren, T. Wittmann, Growth cone advance requires EB1 as revealed by genomic replacement with a light-sensitive variant. *Elife* **12**, (2023).
46. J. Aiken, E. L. F. Holzbaur, Spastin locally amplifies microtubule dynamics to pattern the axon for presynaptic cargo delivery. *bioRxiv*, (2023).
47. A. D. Fellows, M. Bruntraeger, T. Burgold, A. R. Bassett, A. P. Carter, Dynein and dynactin move long-range but are delivered separately to the axon tip. *bioRxiv*, 2023.2007.2003.547521 (2023).
48. B. Nadarajah, J. E. Brunstrom, J. Grutzendler, R. O. Wong, A. L. Pearlman, Two modes of radial migration in early development of the cerebral cortex. *Nat Neurosci* **4**, 143-150 (2001).
49. M. K. Lee, J. B. Tuttle, L. I. Rebhun, D. W. Cleveland, A. Frankfurter, The expression and posttranslational modification of a neuron-specific beta-tubulin isotype during chick embryogenesis. *Cell Motil Cytoskeleton* **17**, 118-132 (1990).
50. A. Ferreira, A. Caceres, Estrogen-enhanced neurite growth: evidence for a selective induction of Tau and stable microtubules. *J Neurosci* **11**, 392-400 (1991).
51. Z. G. Jiang, R. A. Smith, M. M. Neilson, The effects of nerve growth factor on neurite outgrowth from cultured adult and aged mouse sensory neurons. *Brain Res Dev Brain Res* **85**, 212-219 (1995).
52. F. Calderon, H. Y. Kim, Docosahexaenoic acid promotes neurite growth in hippocampal neurons. *J Neurochem* **90**, 979-988 (2004).
53. P. Rana *et al.*, Utilization of iPSC-derived human neurons for high-throughput drug-induced peripheral neuropathy screening. *Toxicol In Vitro* **45**, 111-118 (2017).
54. M. Bershteyn *et al.*, Human iPSC-Derived Cerebral Organoids Model Cellular Features of Lissencephaly and Reveal Prolonged Mitosis of Outer Radial Glia. *Cell Stem Cell* **20**, 435-449 e434 (2017).
55. F. Moya, M. Valdeolmillos, Polarized increase of calcium and nucleokinesis in tangentially migrating neurons. *Cereb Cortex* **14**, 610-618 (2004).
56. A. J. Nichols, L. H. Carney, E. C. Olson, Comparison of slow and fast neocortical neuron migration using a new in vitro model. *BMC Neurosci* **9**, 50 (2008).
57. J. J. Field, J. F. Diaz, J. H. Miller, The binding sites of microtubule-stabilizing agents. *Chem Biol* **20**, 301-315 (2013).
58. A. E. Prota *et al.*, Structural insight into the stabilization of microtubules by taxanes. *Elife* **12**, (2023).
59. G. M. Alushin *et al.*, High-resolution microtubule structures reveal the structural transitions in alphabeta-tubulin upon GTP hydrolysis. *Cell* **157**, 1117-1129 (2014).
60. Z. Cruz-Monserrate *et al.*, Diazonamide A and a synthetic structural analog: disruptive effects on mitosis and cellular microtubules and analysis of their interactions with tubulin. *Mol Pharmacol* **63**, 1273-1280 (2003).
61. H. Ding *et al.*, Electrolytic macrocyclizations: scalable synthesis of a diazonamide-based drug development candidate. *Angew Chem Int Ed Engl* **54**, 4818-4822 (2015).
62. M. Wieczorek *et al.*, The synthetic diazonamide DZ-2384 has distinct effects on microtubule curvature and dynamics without neurotoxicity. *Sci Transl Med* **8**, 365ra159 (2016).
63. T. Cupido, R. Pisa, M. E. Kelley, T. M. Kapoor, Designing a chemical inhibitor for the AAA protein spastin using active site mutations. *Nat Chem Biol* **15**, 444-452 (2019).
64. R. Pisa, T. Cupido, T. M. Kapoor, Designing Allele-Specific Inhibitors of Spastin, a Microtubule-Severing AAA Protein. *J Am Chem Soc* **141**, 5602-5606 (2019).
65. W. Yu *et al.*, The microtubule-severing proteins spastin and katanin participate differently in the formation of axonal branches. *Mol Biol Cell* **19**, 1485-1498 (2008).
66. J. D. Wood *et al.*, The microtubule-severing protein Spastin is essential for axon outgrowth in the zebrafish embryo. *Hum Mol Genet* **15**, 2763-2771 (2006).
67. A. Vemu *et al.*, Severing enzymes amplify microtubule arrays through lattice GTP-tubulin incorporation. *Science* **361**, (2018).
68. C. Hubbert *et al.*, HDAC6 is a microtubule-associated deacetylase. *Nature* **417**, 455-458 (2002).
69. L. Balabanian, C. L. Berger, A. G. Hendricks, Acetylated Microtubules Are Preferentially Bundled Leading to Enhanced Kinesin-1 Motility. *Biophys J* **113**, 1551-1560 (2017).
70. S. Mazzetti *et al.*, Linking acetylated alpha-Tubulin redistribution to alpha-Synuclein pathology in brain of Parkinson's disease patients. *NPJ Parkinsons Dis* **10**, 2 (2024).
71. A. Chazeau, E. A. Katrukha, C. C. Hoogenraad, L. C. Kapitein, Studying neuronal microtubule organization and microtubule-associated proteins using single molecule localization microscopy. *Methods Cell Biol* **131**, 127-149 (2016).

Acknowledgements

We would like to thank Isabelle Sébastien, Jeanette Wihan and Julia Neubauer from the Fraunhofer IBMT, for their excellent support and guidance on the use of NEUR1 neurons throughout the project. We would also like to acknowledge the ABIF facility for their helpful support with data collection. GJB acknowledges support from Natural Sciences and Engineering Research Council of Canada (RGPIN-2014-03791), the Canadian Institutes of Health Research (PJT-148702), and McGill University. AGH is supported by the Canadian Institutes of Health Research (PJT-185997).

Author contributions

Conceptualization and experimental design: MS, Experimental procedures: MS and AP, data analysis: MS and AP, Manuscript initial writing: MS, Manuscript editing: MS, AP, GJB, AGH, Funding acquisition: GJB and AGH.

Competing interest statement

The authors declare no competing interests.

Materials and Methods

NEUR1 iPSC-derived neurons culturing conditions

EBiSC-NEUR1 human-derived neurons were obtained from the European Bank for induced pluripotent Stem Cells (EBiSC) repository. According to the provider's specification sheets, the iPSC donor line BIONi010-C-13 (Sample ID: SAMEA103988285) comes from an African American male donor without any disease phenotype. The iPSC line was initially amplified as embryoid bodies for 2 days. These aggregates were then treated with doxycycline (#D3447, Sigma, 2µg/ml final) for 2 days, and finally dissociated and cryopreserved in Cryostor10 (#07930, Stemcell Technologies) at the repository location. The resulting early neurons were thawed and seeded on PLO/Laminin coated dishes (#P3655, Sigma; #L2020, Sigma). They were grown for 3-7 days in BrainPhys basal media (#05790, Stemcell

Technologies), supplemented with SM1 (#05711, Stemcell Technologies), N2A (#07152, Stemcell Technologies), BDNF (#78005, Stemcell Technologies), GDNF (#78058, Stemcell Technologies), cAMP (#100-0244, Stemcell Technologies) and ascorbic acid (#A5690, Sigma). The doxycycline induction was maintained for 4 days post-thaw. The media was changed every day until treatment, imaging or fixation for further analysis.

Sample preparation, immunofluorescence and immunoblot

For all immunochemistry experiments, on their 3rd day of differentiation in complete BrainPhys, the cells were treated for 7h with the microtubule-targeting drugs. All drugs were used at 10 or 20 times their IC50 and diluted directly in BrainPhys media right before incubation. Paclitaxel (#Y0000698, European Pharmacopeia Reference Standard), trichostatin A (#T1952, Sigma-Aldrich), and DZA (Paraza Pharma, (*61*)) were used at 100nM, while Spastazoline (#SML2659, Sigma-Aldrich) was used at 1µM. For immunofluorescence staining, cells were extracted for 1min30s at 37°C (*71*), before fixation in 4% PFA at 37°C for 15min. The fixed samples were preserved in PBS until staining. For immunoblots, media was removed from cell dishes and 2X Laemmli buffer supplemented with 50nM DTT was directly added to the plates then collected. These crude lysates were sonicated, centrifuged, and boiled for 5min before loading onto gels. Staining and immunoblot procedures were performed as previously described (*40*). Primary antibodies were used as follows: β3-tubulin (#802001, Biolegend) IF 1/500 - WB 1/10000, acetylated α-tubulin 611B1 (#sc23950, Santacruz biotechnologies) IF 1/500 – WB 1/2000, tyrosination YL1/2 (#sc53029, Santacruz biotechnologies) IF 1/50 – WB 1/1000, and polyglutamylation polyE (#AG-25B-0030-C050, Adipogen) IF 1/500 – WB 1/2000. Fluorophore-conjugated secondary antibodies were used at 1/500 while HRP-conjugated ones were used at 1/5000. Nuclei were also stained with DAPI for 5min before mounting of the coverslips with Fluorsave (#345789, Millipore).

Data collection

All microscopes used in this manuscript are part of the McGill University Advanced BioImaging Facility (ABIF), RRID:SCR_017697. The NEUR1 nucleokinesis dataset was acquired on a Zeiss Axio Observer Inverted Widefield Microscope, using the 20X plan apochromat, NA=0.8 air objective. Prior to imaging NEUR1 neurons, 250nM Syto deep red (#S34900, Invitrogen) diluted in BrainPhys was applied to the cells for 20min. The dye was then removed and replaced by 37°C BrainPhys containing the microtubule-targeting drugs or vehicle. Images were taken every 5min for 5-7h. At least 4 independent field of views were recorded per well and each condition was duplicated in the same experiment. Immunofluorescence images were acquired on a Zeiss LSM710 inverted confocal microscope using the 10X plan neofluar NA=0.3 air objective. All images acquired in NEUR1 neurons with or without drugs were acquired in parallel with the same laser power and gain conditions, to allow comparison of the 3 independent experiments.

Analysis

Fiji was used for all image processing and Microsoft Excel and Python were used for graphical representation of the data.

Nuclei tracking. As previously described (*40*), an automated Trackmate-based pipeline built in Fiji was used to generate nuclei tracks for each field of view individually. Maximum linking distance was set up to 20µm, and gaps of 4 frames maximum were allowed. After spot detection by the LoG detector and simple LAP tracking, all the trajectories were compiled for further analysis in python. The mean speed, distance travelled, displacement and directionality index (Displacement divided by distance travelled (*40*)) were directly obtained from Trackmate. Only tracks that lasted more than 30min were included in the quantifications (75% of all tracks).

Neurite extension. To measure the average arborization length per cell, we used the Tubb3 and DAPI immunofluorescence stainings. After filtering and thresholding of both channels, the Tubb3 channel was skeletonized. The fraction of the image covered by the skeleton was divided by the number of nuclei picked up by the "Analyze particles" plugin in Fiji.

Quantification of tubulin/PTMs. After filtering and binarization of the Tubb3 channel, it was used as a mask to determine the neurons' locations. The signal intensity for the other channels were measured within the masked region and normalized to the Tubb3 intensity in the mask.

Quantification of nucleus AR. The aspect ratio for all nuclei was measured from the DAPI channel images using the shape descriptors option of the "Analyze particles" plugin.

Statistics

All statistical tests used are indicated in the figure legends: Kruskal-Wallis non parametric H test, or Mann-Whitney non parametric U test. P values were considered nonsignificant when above 0.05. Whenever data was not showed on plots, it was specified in figure captions.

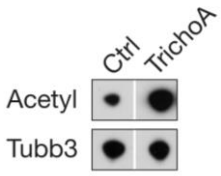

Figure S1: Microtubule acetylation levels. Representative immunoblot showing the increase in acetylation upon treatment with Trichostatin A. Control and Trichostatin samples are on the same membrane, and they were exposed together for the same amount of time.